



Full strain tensor measurements with X-ray diffraction and strain field mapping: a simulation study

M. X. Tang,^{a,b} J. W. Huang,^a J. C. E,^c Y. Y. Zhang^{a*} and S. N. Luo^{a,b*}

^aThe Peac Institute of Multiscale Sciences, Chengdu, Sichuan 610031, People's Republic of China, ^bKey Laboratory of Advanced Technologies of Materials, Ministry of Education, and Institute of Material Dynamics, Southwest Jiaotong University, Chengdu, Sichuan 610031, People's Republic of China, and ^cEuropean XFEL GmbH, 22869 Schenefeld, Germany. *Correspondence e-mail: yzhang@pims.ac.cn, sluo@pims.ac.cn

Received 26 September 2019

Accepted 18 March 2020

Edited by M. Yamamoto, RIKEN Spring-8 Center, Japan

Keywords: strain tensor; X-ray diffraction; strain field; 2D diffraction ring fitting; material strength.

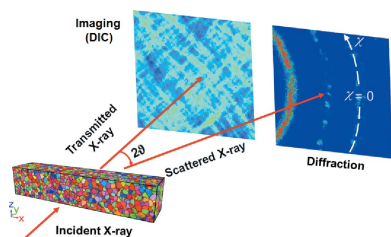
Strain tensor measurements are important for understanding elastic and plastic deformation, but full bulk strain tensor measurement techniques are still lacking, in particular for dynamic loading. Here, such a methodology is reported, combining imaging-based strain field mapping and simultaneous X-ray diffraction for four typical loading modes: one-dimensional strain/stress compression/tension. Strain field mapping resolves two in-plane principal strains, and X-ray diffraction analysis yields volumetric strain, and thus the out-of-plane principal strain. This methodology is validated against direct molecular dynamics simulations on nanocrystalline tantalum. This methodology can be implemented with simultaneous X-ray diffraction and digital image correlation in synchrotron radiation or free-electron laser experiments.

1. Introduction

The strain tensor is vital for characterizing mechanical properties of materials, understanding elastic and plastic deformation mechanisms, and developing physics-based constitutive models (Milathianaki *et al.*, 2013; Allais *et al.*, 1994; Poulsen *et al.*, 2005; Zhu *et al.*, 2017). However, it is still a challenge to measure the full bulk strain tensor, especially for fast or ultrafast dynamic experiments. The development of advanced X-ray sources such as synchrotron radiation sources and X-ray free-electron lasers (XFELs) offers the opportunity to capture *in situ* dynamic events (Luo *et al.*, 2012; Milathianaki *et al.*, 2013; Wehrenberg *et al.*, 2017; Seiboth *et al.*, 2018; Coleman *et al.*, 2019; Brown *et al.*, 2019; Huang *et al.*, 2016a,b; Fan *et al.*, 2016; Turneure *et al.*, 2017; Briggs *et al.*, 2019), including strain and X-ray diffraction measurements.

High-speed X-ray phase contrast imaging (Lu *et al.*, 2017; Huang *et al.*, 2016b) is utilized to obtain two-dimensional (2D) strain fields via digital image correlation (DIC) (Lu *et al.*, 2014, 2016). However, the 2D strain field is only mapped on the plane perpendicular to the incident X-ray beam (in-plane strain components), and strains along the incident direction cannot be resolved. On the other hand, high-speed X-ray diffraction usually provides lattice strain measurements (Ma *et al.*, 2017; Zhang *et al.*, 2017; Collins *et al.*, 2015).

Given the 2D nature of in-plane strain field mapping, the missing bulk strain components have to be obtained via other means such as X-ray diffraction. X-ray Laue microdiffraction or Laue DIC (Petit *et al.*, 2015), suitable for up to hundreds of grains, was applied to measure the local strain tensor, but these quasi-static techniques can hardly be used for highly transient events. A recent study (Zhang *et al.*, 2019) demonstrated that equivalent volumetric strain can be obtained



under 1D strain loading conditions or planar shock compression via analysis of 2D diffraction patterns; however, all the principal strain components cannot be resolved. It is highly desirable to develop techniques to obtain the full bulk strain tensor in dynamic experiments.

For bulk strain tensor measurements (in particular under short time scale dynamic loading), we propose a methodology combining 2D strain mapping and X-ray analysis of 2D diffraction patterns: the former resolves two in-plane principal strains via imaging, and the latter volumetric strain (thus the out-of-plane principal strain). We validate this methodology against direct molecular dynamics (MD) simulations on nanocrystalline tantalum under four typical loading modes. This methodology can be implemented with simultaneous X-ray diffraction and DIC in synchrotron radiation or free-electron laser experiments.

This article is organized as follows. Section 2 addresses the methodology of simulated experimental geometry, MD simulations, strain field mapping and the Singh analysis of 2D diffraction patterns; Section 3 presents results and discussion, validating the strain measurements against direct MD simulations, and Section 4 presents conclusion.

2. Methodology

2.1. Simulated experimental geometry

The simulation geometry for simultaneous diffraction and imaging measurements is presented in Fig. 1 as in experiments (Lu *et al.*, 2016). The loading direction is along the x -axis, while the incident X-ray beam is along the y -axis. We use the transmission geometry for diffraction simulations. Here a 2D detector is set perpendicular to the incident X-ray direction (the normal detector position); for an arbitrary detector position, a geometrical correction can be applied.

In experiments, the strain field is mapped onto the plane perpendicular to the incident X-ray beam (the y -axis), normally done via X-ray DIC with phase contrast imaging (Lu

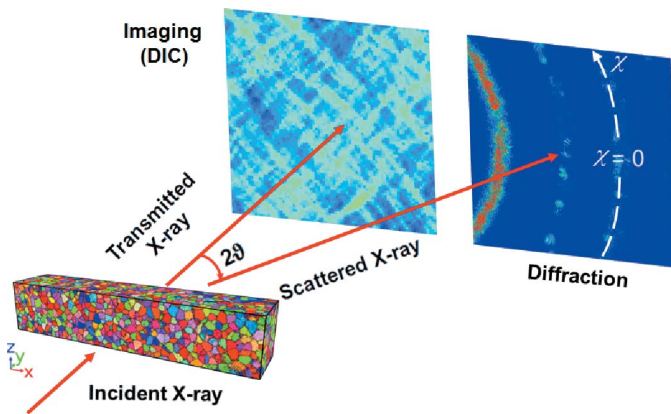


Figure 1
Schematic illustrating simultaneous X-ray imaging (for strain mapping) and diffraction in the transmission mode. DIC: digital image correlation. 2θ : diffraction angle; χ : azimuthal angle.

et al., 2014). Here we obtain strain fields on the xz -plane from atomic positions in MD trajectories (see below), to mimic X-ray DIC measurement.

2.2. Molecular dynamics simulations

For MD simulations, we use the large-scale Atomic/Molecular Massively Parallel Simulator (Plimpton, 1995) and a widely used embedded-atom method (EAM) potential (Ravelo *et al.*, 2013) for tantalum. This EAM potential is accurate for describing the properties of tantalum as shown by numerous shock (Wang *et al.*, 2014; Tang *et al.*, 2018; Hahn *et al.*, 2017) and nonshock simulations (Remington *et al.*, 2014; Huang *et al.*, 2017).

We construct a nanocrystalline tantalum configuration with dimensions of about $200 \text{ nm} \times 40 \text{ nm} \times 40 \text{ nm}$, corresponding to 17.5 million atoms. This configuration contains about 2500 grains, and the average grain size is about 5 nm. Four loading modes commonly encountered in experiments are simulated: compression and tension under 1D strain conditions as in planar shock compression, and compression and tension under 1D stress conditions as in materials testing systems, referred to as 1D-strain compression, 1D-strain tension, 1D-stress compression, and 1D-stress tension, respectively. Prior to loading, the configuration is relaxed at 0 K, and then annealed with the constant-pressure-temperature ensemble under 3D periodic boundary conditions at 300 K and zero pressure (Wang *et al.*, 2016).

For 1D-strain compression/tension loading, the relaxed nanocrystalline configuration is compressed/stretched along the x -axis, and the microcanonical ensemble is used to mimic adiabatic loading as in shock compression. The dimension along the x -axis is reduced/increased at a fixed decrement/increment, corresponding to a strain rate of 10^9 s^{-1} (Speart *et al.*, 2007; Tschoop & McDowell, 2008). For 1D-stress compression/tension loading, the configuration dimension along the x -axis is changed under a constant strain rate of 10^9 s^{-1} , while the stress-free boundary condition is applied along the y - and z -axes (Speart *et al.*, 2007). The temperature is set at 300 K.

All the loading simulations are conducted under 3D periodic boundary conditions. The time step for integration of the equation of motion is 1 fs. Physical quantities such as particle velocity, density, stress, and temperature can be obtained from trajectories via binning analysis (Luo *et al.*, 2009).

Stress tensor can be decomposed into hydrostatic and deviatoric stress components as

$$\begin{pmatrix} \sigma_{xx} & 0 & 0 \\ 0 & \sigma_{yy} & 0 \\ 0 & 0 & \sigma_{zz} \end{pmatrix} = \sigma_p \mathbf{I} + \begin{pmatrix} \frac{2}{3}t & 0 & 0 \\ 0 & -\frac{1}{3}t & 0 \\ 0 & 0 & -\frac{1}{3}t \end{pmatrix},$$

where \mathbf{I} is the identity matrix, $\sigma_{xx} \geq \sigma_{yy} = \sigma_{zz}$ for homogeneous isotropic solids, $\sigma_p = (1/3)(\sigma_{xx} + \sigma_{yy} + \sigma_{zz})$ represents the mean normal stress or so-called equivalent hydrostatic stress, and $t = \sigma_{xx} - (1/2)(\sigma_{yy} + \sigma_{zz})$ denotes the differential stress.

The bulk strain tensor, ε_{ij} ($i, j = x, y, z$), can be obtained from the dimension (L_i) and shape changes of a whole simu-

lation cell (Method I). The normal engineering strains are determined from the dimension changes as

$$\varepsilon_{ii} = \frac{\Delta L_i}{L_i} \quad \text{with } i = x, y, z. \quad (1)$$

Shear strain components are the change of the angles between edges of the whole simulation cell, and equal zero for the four common loading modes investigated in this work.

2.3. Strain field mapping and analysis

For strain field mapping, we take two atomic configurations from MD simulations, the reference (0 ps; undeformed) and current configurations (e.g. 80 ps; deformed). For each atom m , we calculate the atomic strain tensor (Stukowski, 2010) as $\varepsilon_{ij}^m = (1/2)(u_{i,j}^m + u_{j,i}^m)$ ($i, j = x, y, z$). u^m is the atomic displacement of the m th atom and ε_{ij}^m essentially represents the 3D strain field around this atom.

The average atomic strain tensor for N atoms or bulk strain tensor follows as

$$\varepsilon_{ij} = \frac{1}{2N} \sum_{m=1}^N (u_{i,j}^m + u_{j,i}^m). \quad (2)$$

This method for calculating bulk engineering strain is referred to as Method II. Then we calculate the volumetric strain (ε_p) as follows,

$$\varepsilon_p = (1 + \varepsilon_{xx})(1 + \varepsilon_{yy})(1 + \varepsilon_{zz}) - 1. \quad (3)$$

In experiments, only the 2D engineering strain tensor (Method III) can be obtained via the projection along an imaging direction. In addition, the strain tensor is often expressed in terms of the Green–Lagrange strain tensor [Lu *et al.*, 2014; Stukowski, 2010]. We thus also calculate the Green–Lagrange strain for each atom m ,

$$E_{ij}^m = \frac{1}{2} (u_{i,j}^m + u_{j,i}^m + u_{k,i}^m u_{k,j}^m), \quad (4)$$

with $i, j, k = x, y, z$. E_{ij}^m is then projected along the y -axis to obtain the 2D Green–Lagrange strain field. Note that E_{ij}^m and ε_{ij}^m are equivalent for describing strain field, and can be converted from one to the other (Lu *et al.*, 2014; Stukowski, 2010).

2.4. X-ray diffraction simulations and analysis

Atomic configurations from MD simulations are used as input to diffraction calculations with *GAPD*, a *GPU-accelerated Atom-based Polychromatic Diffraction* simulation code (E *et al.*, 2018). The scattered X-ray intensity is calculated in 3D reciprocal space, and then projected onto a 2D detector to obtain diffraction patterns as in experiments. Diffraction angle (2ϑ) and azimuthal angle (χ) are defined in Fig. 1, and the loading direction (the x -axis) forms an angle of θ with the normal of a diffracting plane under consideration. θ is referred to as the loading–diffraction geometry angle (Zhang *et al.*, 2019), and can be varied as desired. There exists the following relation among θ , 2ϑ , and χ under simulated geometry,

$$\cos \theta = \cos \vartheta \cos \chi. \quad (5)$$

The X-ray wavelength in our calculations is 0.512 Å (24.22 keV), the peak intensity wavelength of the undulator source with a period of 18 mm and a gap of 12 mm at 32ID-B of the Advanced Photon Source. Simulated 2ϑ ranges from 10° to 30°, and the corresponding range of θ is 5°–90°.

From 2D X-ray diffraction patterns, we can deduce the bulk density under the equivalent hydrostatic pressure (σ_p) and residual strength (Singh, 1993; Zhang *et al.*, 2019). The methodology has been demonstrated to be appropriate for 1D-strain compression including shock compression (Zhang *et al.*, 2019). The measured lattice spacing, $d_m(hkl)$, is related to θ via

$$d_m(hkl) = d_p(hkl)[1 + (1 - 3 \cos^2 \theta)Q(hkl)]. \quad (6)$$

Here, $d_p(hkl)$ denotes d -spacing due to σ_p , and $Q(hkl)$ is a factor which depends on t and single-crystal elastic compliances. Since $d_m = \lambda/(2 \sin \vartheta)$, we obtain a scatter plot of d_m versus $(1 - 3 \cos^2 \theta)$, which can then be fitted with equation (6). More analysis details have been presented elsewhere (Zhang *et al.*, 2019).

Given $d_p(hkl)$ determined from 2D diffraction patterns, we have $\varepsilon_p = [d_p(hkl)/d_0(hkl)]^3 - 1$. Since ε_{xx} and ε_{zz} are evaluated from strain field mapping, the unknown tensor component ε_{yy} can be solved with equation (3), and the full strain tensor, determined by virtue of a combination of 2D strain field mapping (imaging) and diffraction patterns (Method IV). Method IV is experimentally feasible for full strain tensor measurements.

3. Results and discussion

3.1. MD simulations

We explore the four most common loading modes in high-pressure experiments and mechanical testing: 1D-strain compression, 1D-strain tension, 1D-stress compression, and 1D-stress tension. The initial configurations are the same for these loading modes. The stress–strain curves directly obtained from MD simulations are shown in Fig. 2, including normal stress (σ_{xx}), equivalent hydrostatic stress (σ_p), and differential stress (t). As an example, the full strain tensor ε_{ij} and volumetric strain ε_p at $\varepsilon_{xx} = 8.00\%$, calculated directly from the simulation cell dimensions/shapes (Method I), are presented in Table 1 for the four loading modes.

For 1D-strain compression [Fig. 2(a)], σ_{xx} increases to about 71.0 GPa, and σ_p increases to about 68.0 GPa as bulk loading strain ε_{xx} increases to 20.00%, while t increases to 5.2 GPa at $\varepsilon_{xx} = 9.00\%$ and then decreases to 4.2 GPa due to yield. σ_p is slightly less than σ_{xx} . For 1D-strain tension [Fig. 2(b)], as strain ε_{xx} reaches 9.00%, voids nucleate in the sample and tensile failure occurs. σ_{xx} and σ_p reach their peak values (15.2 GPa and 12.5 GPa, respectively) at about $\varepsilon_{xx} = 9.50\%$, while t peaks at $\varepsilon_{xx} = 8.50\%$ (4.4 GPa).

Different from the 1D-strain compression, σ_{xx} in 1D-stress compression [Fig. 2(c)] reaches a much lower peak value of

Table 1

Bulk strain tensor (ϵ_{ij}) and volumetric strain (ϵ_p) for the four loading modes with $\epsilon_{xx} = 8.00\%$.

The off-diagonal values of ϵ_{ij} are zero and thus not shown. Method I: based on dimension and shape changes of a simulation cell; Method II: based on 3D strain field mapping; Method III: based on 2D strain mapping; Method IV: based on 2D strain field mapping combined with analysis of 2D X-ray diffraction patterns.

	Strain (%)			
	Method I	Method II	Method III	Method IV
1D strain compression				
ϵ_{xx}	-8.00	-8.08	-8.08	-8.08
ϵ_{yy}	0.00	0.16	-	0.16
ϵ_{zz}	0.00	0.16	0.16	0.16
ϵ_p	-8.00	-7.79	-	-7.79
1D strain tension				
ϵ_{xx}	8.00	7.90	7.90	7.90
ϵ_{yy}	0.00	-0.10	-	0.10
ϵ_{zz}	0.00	-0.10	-0.10	-0.10
ϵ_p	8.00	7.68	-	7.90
1D stress compression				
ϵ_{xx}	-8.00	-8.06	-8.06	-8.06
ϵ_{yy}	3.80	3.62	-	4.19
ϵ_{zz}	3.82	3.65	3.65	3.65
ϵ_p	-0.86	-1.25	-	-0.71
1D stress tension				
ϵ_{xx}	8.00	7.80	7.80	7.80
ϵ_{yy}	-3.28	-3.40	-	-2.82
ϵ_{zz}	-3.35	-3.46	-3.46	-3.46
ϵ_p	0.96	0.53	-	1.14

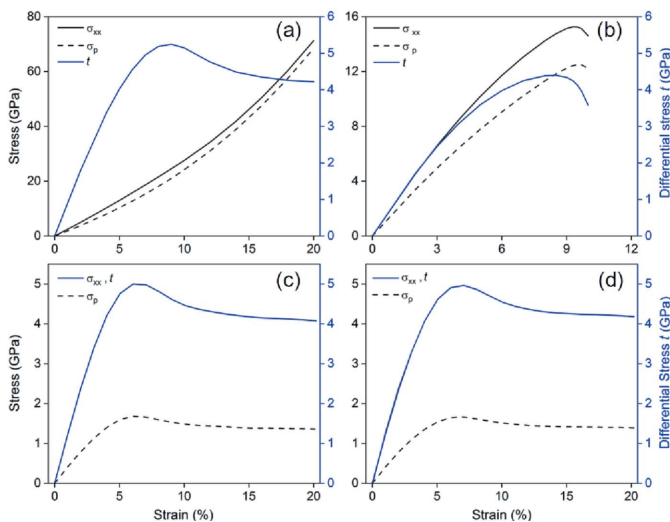


Figure 2

Bulk stress-strain curves for four representative loading modes: (a) 1D-strain compression, (b) 1D-strain tension, (c) 1D-stress compression and (d) 1D-stress tension. For better visualization, the absolute values of tensile stresses are used for plotting.

5.1 GPa at $\epsilon_{xx} = 6.00\%$, and t is the same as σ_{xx} due to the lack of lateral confinement (stress-free along the y - and z -axes), and $\sigma_p = (1/3)\sigma_{xx}$. For 1D-stress tension [Fig. 2(d)], σ_{xx} and t reach a peak stress of 5.0 GPa at $\epsilon_{xx} = 6.00\%$, and $\sigma_p = (1/3)\sigma_{xx}$.

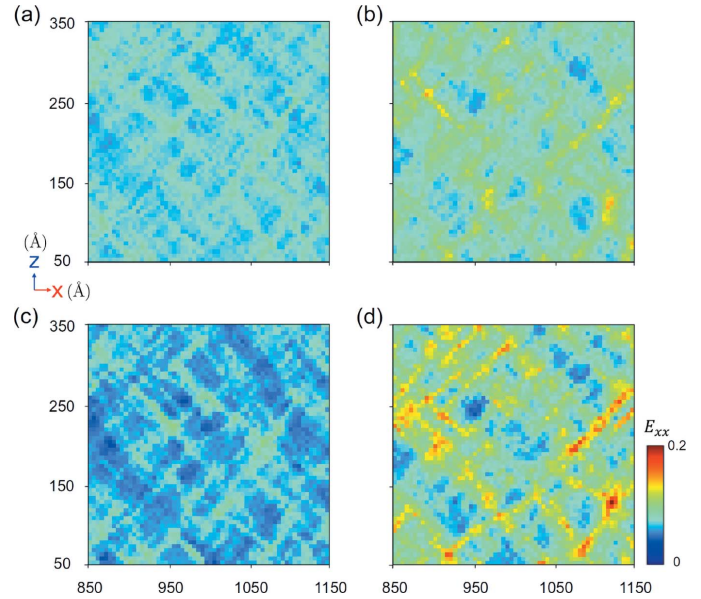


Figure 3

Green-Lagrange strain fields of E_{xx} for four deformation modes with bulk strain component $\epsilon_{xx} = 8.00\%$: (a) 1D-strain compression, (b) 1D-strain tension, (c) 1D-stress compression, and (d) 1D-stress tension. Color coding is based on E_{xx} .

3.2. Strain field mapping

3D strain field maps are obtained from two atomic configurations (Method II). Since the Green-Lagrange strain field is measured with X-ray phase contrast imaging in experiments, we also calculate 2D Green-Lagrange strain field maps via 2D binning along the x - and z -axes of the 3D strain maps. We select the central regions of about $300 \text{ \AA} \times 300 \text{ \AA}$ for visualization (Fig. 3; bulk strain $\epsilon_{xx} = 8.00\%$).

Strain is more localized at grain boundaries than in grain interiors, and under 1D-stress loading than under 1D-strain loading (Fig. 3). Strain inhomogeneity and strain at grain boundaries are higher under tension than under compression [Figs. 3(b) and 3(d)].

From 3D and 2D strain maps, we can calculate bulk strain tensor components ϵ_{ij} and volumetric strain (ϵ_p). Methods II and III yield accurate results compared with Method I (Table 1). However, ϵ_{yy} and ϵ_p cannot be obtained with Method III, which on the other hand can be obtained from analysis of 2D X-ray diffraction patterns.

3.3. X-ray diffraction

1D X-ray diffraction profiles are most commonly used to obtain d -spacing and lattice strain of corresponding diffracting planes. The $\{110\}$ lattice strains are calculated from the 1D diffraction curves for the four loading modes (Fig. 4), and listed in Table 2.

However, lattice strain is not necessarily equal to bulk strain; their relation depends on sample microstructure, diffraction geometry, and stress conditions. For example, for the same bulk strain $\epsilon_{xx} = 8.00\%$, the shift of 2θ is much bigger under 1D-strain loading than that under 1D-stress loading

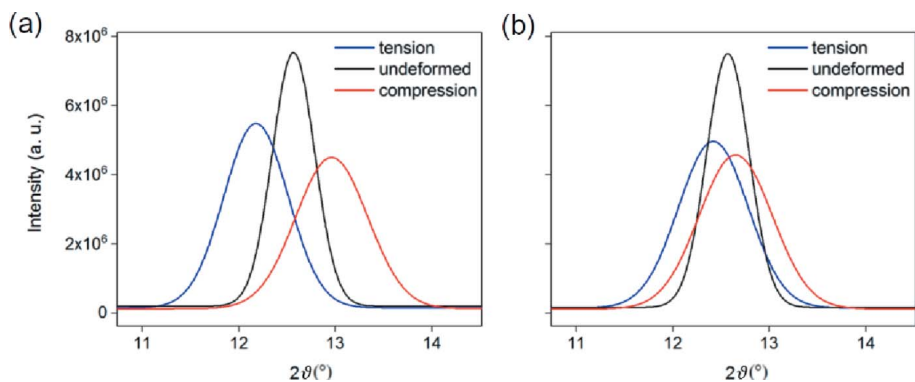


Figure 4 [110] diffraction profiles for (a) 1D-strain compression and tension, and (b) 1D-stress compression and tension.

Table 2

Diffraction angles (2ϑ), interplanar spacings (d) and lattice strains (ε_l) for the {110} diffraction peak calculated from 1D diffraction profiles for bulk strain $\varepsilon_{xx} = 8.00\%$.

Subscript 0 refers to undeformed.

Loading modes	$2\vartheta_0$	2ϑ	d_0 (Å)	d (Å)	ε_l
1D-strain compression	12.57°	12.96°	2.338	2.268	-3.00%
1D-strain tension	12.57°	12.18°	2.338	2.413	3.21%
1D-stress compression	12.57°	12.65°	2.338	2.324	-0.60%
1D-stress tension	12.57°	12.42°	2.338	2.367	1.24%

(Table 2). If we assume hydrostatic deformation, the bulk volumetric strains [$\varepsilon_p = (d/d_0)^3 - 1$] would be -8.70%, 9.94%, -1.79% and 3.77%, for 1D-strain compression and tension, and 1D-stress compression and tension, respectively. The corresponding bulk volumetric strains directly obtained from MD simulations are considerably different, being -8.00%, 8.00%, -0.86% and 0.96%. Thus, such simplified analyses of 1D diffraction curves are inappropriate.

2D diffraction patterns allow one to extract more information with high accuracy on the basis of the Singh theory (Singh, 1993), including differential stress (or residual strength) and equivalent hydrostatic strain under nonhydrostatic conditions (Zhang *et al.*, 2019). Fig. 5(a) shows three major diffraction rings, {110}, {200}, and {112}, for 1D-strain compression with $\varepsilon_{xx} = 8.00\%$. The strongest {110} ring is used for the analysis with the Singh theory, and the results are shown in Fig. 5(c). We obtain $d_p = 2.276$ Å, and thus the equivalent hydrostatic volumetric strain is -7.79%. The residual strength is obtained to be $t = 5.34$ GPa, with the aggregate shear modulus G calculated directly from MD simulations. The corresponding values directly from MD simulations are $\varepsilon_p = -8.00\%$ and $t = 5.19$ GPa (Table 3), which agree with the analysis of 2D diffraction patterns. For other loading modes, the agreement between direct MD simulations and the analysis of 2D diffraction patterns (Table 3) is also reasonable. Thus, the

Singh analysis can be used for obtaining bulk volumetric strain for different loading modes.

In certain experiments, it is unfeasible to obtain full diffraction rings due to physical constraints. We explore below whether/how partial diffraction rings can be used for accurate measurements. As an example, we select 1/4 of the {110} diffraction rings (χ spans over 0–45° and 315°–360°) for analysis [Fig. 5(b)]. The Singh analysis [Fig. 5(d)] yields a volumetric strain of about -7.14% and residual strength of about 6.27 GPa, as opposed to -7.79% and 5.34 GPa obtained from the full diffraction rings.

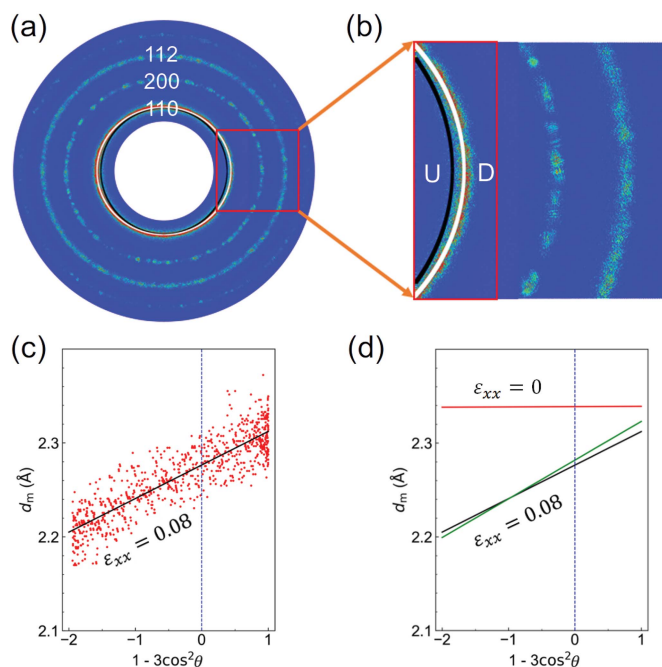


Figure 5

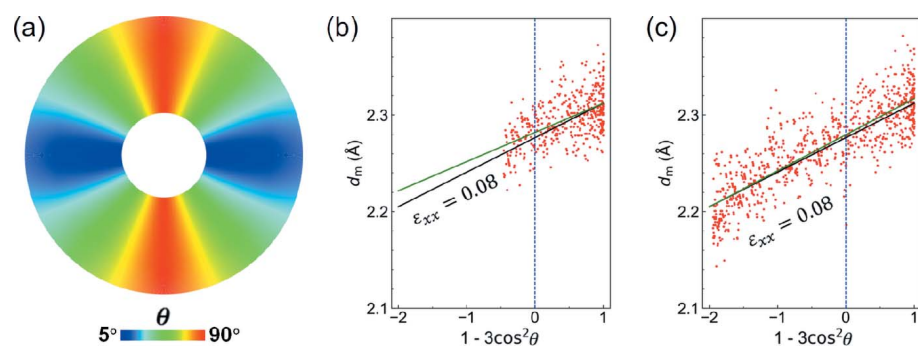
Diffraction analysis with full and partial diffraction rings. For the latter, χ spans over 0–45° and 315°–360°. (a) Full diffraction rings of tantalum under uniaxial strain compression ($\varepsilon_{xx} = 0.08$), and (b) corresponding partial diffraction rings. White curves: deformed (D); black curves: undeformed (U). (c) d_m versus $(1 - 3 \cos^2 \theta)$ plot for the full {110} diffraction ring. Red dots: ‘data,’ black line: linear fitting. (d) Comparison of the d_m versus $(1 - 3 \cos^2 \theta)$ plots for fitting with full (black curve) and partial (green) {110} diffraction rings.

Table 3

Fitting to full {110} diffraction rings for $\varepsilon_{xx} = 8.00\%$.

Subscripts 1 and 2 refer to MD results and the Singh analysis of diffraction patterns, respectively.

Loading modes	d_p (Å)	Q	t_1 (GPa)	t_2 (GPa)	ε_{p1}	ε_{p2}
1D-strain compression	2.276	0.0157	5.19	5.34	-8.00%	-7.79%
1D-strain tension	2.399	-0.0146	-4.38	-4.48	8.00%	7.90%
1D-stress compression	2.333	0.0151	4.98	4.99	-0.86%	-0.71%
1D-stress tension	2.348	-0.0153	-4.90	-4.71	0.96%	1.14%


Figure 6

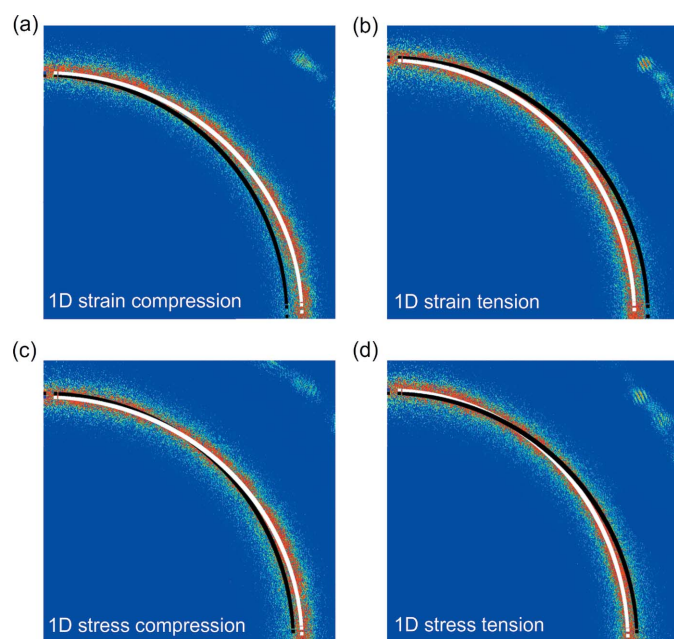
(a) Distribution of θ on the detector plane for the simulated geometry. (b) Fitting for the $\{110\}$ diffraction ring with $45^\circ \leq \chi \leq 135^\circ$. (c) Fitting for the $\{110\}$ diffraction ring with $0^\circ \leq \chi \leq 90^\circ$. Black and green lines: full and partial diffraction rings, respectively; red dots: 'data.'

Table 4

Fitting to partial $\{110\}$ diffraction rings for $\varepsilon_{xx} = 8.00\%$.

Subscripts 1 and 2 refer to MD results and the Singh analysis of diffraction patterns, respectively.

Loading modes	d_p (Å)	Q	t_1 (GPa)	t_2 (GPa)	ε_{p1}	ε_{p2}
1D-strain compression	2.279	0.0164	5.19	5.58	-8.00%	-7.41%
1D-strain tension	2.396	-0.0142	-4.38	-4.35	8.00%	7.49%
1D-stress compression	2.334	0.0157	4.98	5.17	-0.86%	-0.55%
1D-stress tension	2.346	-0.0164	-4.90	-5.05	0.96%	0.99%


Figure 7

$\{110\}$ diffraction rings of nanocrystalline tantalum under (a) 1D-strain compression, (b) 1D-strain tension, (c) 1D-stress compression, and (d) 1D-stress tension loading. Black and white curves: fittings to simulated diffraction rings for the undeformed and deformed ($\varepsilon_{xx} = 8.00\%$) cases, respectively.

The significant differences are due to the fact that the θ -range corresponding to the selected χ -range is 5° – 45° [Fig. 6(a)] and not representative. Similarly, for $45^\circ \leq \chi < 135^\circ$, θ ranges from 45° to 90° ; as a result, the d_m versus $1 - 3\cos^2\theta$ scatter plot

only spans a partial range, so the linear fitting is not well constrained [Fig. 6(b)]. On the other hand, a properly chosen χ -range, e.g. 0° – 90° , can cover a much wider/whole θ -range (5° – 90°). Consequently, the fitting is much better and in agreement with that using the full diffraction ring [Fig. 6(c)].

With a properly chosen χ -range, we analyze partial $\{110\}$ diffraction rings ($0^\circ \leq \chi \leq 90^\circ$, Fig. 7) for four loading modes with $\varepsilon_{xx} = 8.00\%$. Their corresponding fittings with equation (6) show different features (shapes and shifts in 2ϑ). The fitting results of t and ε_p (Table 4) show that the direct simulations agree with the Singh analysis for these four loading modes. Note that, for 1D-stress loading, equivalent hydrostatic strains are much smaller compared with the applied strain $\varepsilon_{xx} = 8.00\%$ due to the Poisson's effect.

The Singh analysis of partial/full 2D diffraction patterns yields bulk volumetric strain (equivalent hydrostatic strain, ε_p). In addition, two strain

components ε_{xx} and ε_{zz} can be obtained from strain field mapping, e.g. via X-ray DIC. Then, ε_{yy} can be calculated with equation (3), and the full strain tensor obtained for these loading modes.

In experiments, strain fields can be obtained via DIC with X-ray phase contrast imaging or optical imaging, and along with simultaneous X-ray diffraction, full strain tensors can be obtained for the most common loading modes. Both imaging and diffraction can be carried out at the single-bunch level at synchrotrons or XFELs (Luo *et al.*, 2012; Lu *et al.*, 2016; Seiboth *et al.*, 2018). Thus, Method IV can be implemented for *in situ*, real-time, dynamic synchrotron or XFEL experiments.

4. Conclusions

We have developed a methodology of bulk strain tensor measurements for four typical loading modes, 1D strain/stress compression/tension, via a combination of imaging-based strain field mapping and simultaneous X-ray diffraction. Strain field mapping measures two in-plane principal strains (ε_{xx} and ε_{zz}); X-ray diffraction analysis yields volumetric strain, and thus the out-of-plane principal strain (ε_{yy}). This methodology is validated against direct molecular dynamics simulations on nanocrystalline tantalum, and can be implemented with simultaneous X-ray diffraction and digital image correlation in synchrotron radiation or free-electron laser experiments.

Acknowledgements

The computations were performed at the Supercomputing Center of the Peac Institute of Multiscale Sciences.

Funding information

Funding for this research was provided by: Scientific Challenge Project of China (grant No. TZ2018001); National NaturalScience Foundation of China (grant No. 11627901).

References

Allais, L., Bornert, M., Bretheau, T. & Caldemaison, D. (1994). *Acta Metall. Mater.* **42**, 3865–3880.

Briggs, R., Torchio, R., Sollier, A., Ocelli, F., Videau, L., Kretzschmar, N. & Wulff, M. (2019). *J. Synchrotron Rad.* **26**, 96–101.

Brown, S. B., Gleason, A. E., Galtier, E., Higginbotham, A., Arnold, B., Fry, A., Granados, E., Hashim, A., Schroer, C. G., Schropp, A., Seiboth, F., Tavella, F., Xing, Z., Mao, W., Lee, H. J. & Nagler, B. (2019). *Sci. Adv.* **5**, eaau8044.

Coleman, A. L., Gorman, M. G., Briggs, R., McWilliams, R. S., McGonegle, D., Bolme, C. A., Gleason, A. E., Fratanduono, D. E., Smith, R. F., Galtier, E., Lee, H. J., Nagler, B., Granados, E., Collins, G. W., Eggert, J. H., Wark, J. S. & McMahon, M. I. (2019). *Phys. Rev. Lett.* **122**, 255704.

Collins, D. M., Mostafavi, M., Todd, R. I., Connolley, T. & Wilkinson, A. J. (2015). *Acta Mater.* **90**, 46–58.

E, J. C., Wang, L., Chen, S., Zhang, Y. Y. & Luo, S. N. (2018). *J. Synchrotron Rad.* **25**, 604–611.

Fan, D., Huang, J. W., Zeng, X. L., Li, Y. E. J. C., Huang, J. Y., Sun, T., Fezzaa, K., Wang, Z. & Luo, S. N. (2016). *Rev. Sci. Instrum.* **87**, 053903.

Hahn, E. N., Germann, T. C., Ravelo, R., Hammerberg, J. E. & Meyers, M. A. (2017). *Acta Mater.* **126**, 313–328.

Huang, C., Peng, X., Fu, T., Chen, X., Xiang, H., Li, Q. & Hu, N. (2017). *Mater. Sci. Eng. A*, **700**, 609–616.

Huang, J. W., E, J. C., Huang, J. Y., Sun, T., Fezzaa, K. & Luo, S. N. (2016a). *J. Synchrotron Rad.* **23**, 712–717.

Huang, J. Y., Huang, J. W., Sun, T., Fezzaa, K., Xu, S. L. & Luo, S. N. (2016b). *Acta Mater.* **114**, 136–145.

Lu, L., Fan, D., Bie, B. X., Ran, X. X., Qi, M. L., Parab, N., Sun, J. Z., Liao, H. J., Hudspeth, M. C., Claus, B., Fezzaa, K., Sun, T., Chen, W., Gong, X. L. & Luo, S. N. (2014). *Rev. Sci. Instrum.* **85**, 076101.

Lu, L., Huang, J. W., Fan, D., Bie, B. X., Sun, T., Fezzaa, K., Gong, X. L. & Luo, S. N. (2016). *Acta Mater.* **120**, 86–94.

Lu, L., Sun, T. K. K. F., Fezzaa, K., Gong, X. L. & Luo, S. N. (2017). *Mater. Sci. Eng. A*, **701**, 143–148.

Luo, S. N., An, Q., Germann, T. C. & Han, L. B. (2009). *J. Appl. Phys.* **106**, 013502.

Luo, S. N., Jensen, B. J., Hooks, D. E., Fezzaa, K., Ramos, K. J., Yeager, J. D., Kwiatkowski, K. & Shimada, T. (2012). *Rev. Sci. Instrum.* **83**, 073903.

Ma, L., Wang, L., Nie, Z., Wang, F., Xue, Y., Zhou, J., Cao, T., Wang, Y. & Ren, Y. (2017). *Acta Mater.* **128**, 12–21.

Milathianaki, D., Boutet, S., Williams, G. J., Higginbotham, A., Ratner, D., Gleason, A. E., Messerschmidt, M., Seibert, M. M., Swift, D. C., Hering, P., Robinson, J., White, W. E. & Wark, J. S. (2013). *Science*, **342**, 220–223.

Petit, J., Castelnaud, O., Bornert, M., Zhang, F. G., Hofmann, F., Korsunsky, A. M., Faurie, D., Le Bourlot, C., Micha, J. S., Robach, O. & Ulrich, O. (2015). *J. Synchrotron Rad.* **22**, 980–994.

Plimpton, S. (1995). *J. Comput. Phys.* **117**, 1–19.

Poulsen, H. F., Wert, J. A., Neufeind, J., Honkimäki, V. & Daymond, M. (2005). *Nat. Mater.* **4**, 33–36.

Ravelo, R., Germann, T. C., Guerrero, O., An, Q. & Holian, B. L. (2013). *Phys. Rev. B*, **88**, 134101.

Remington, T. P., Ruestes, C. J., Bringa, E. M., Remington, B. A., Lu, C. H., Kad, B. & Meyers, M. A. (2014). *Acta Mater.* **78**, 378–393.

Seiboth, F., Fletcher, L. B., McGonegle, D., Anzellini, S., Dresselhaus-Cooper, L. E., Frost, M., Galtier, E., Goede, S., Harmand, M., Lee, H. J., Levitan, A. L., Miyanishi, K., Nagler, B., Nam, I., Ozaki, N., Rödel, M., Schropp, A., Spindloe, C., Sun, P., Wark, J. S., Hastings, J., Glenzer, S. H. & McBride, E. E. (2018). *Appl. Phys. Lett.* **112**, 221907.

Singh, A. K. (1993). *J. Appl. Phys.* **73**, 4278–4286.

Spearot, D. E., Tschopp, M. A., Jacob, K. I. & McDowell, D. L. (2007). *Acta Mater.* **55**, 705–714.

Stukowski, A. (2010). *Modell. Simul. Mater. Sci. Eng.* **18**, 015012.

Tang, M. X., Zhang, Y. Y., E, J. C. & Luo, S. N. (2018). *J. Synchrotron Rad.* **25**, 748–756.

Tschopp, M. A. & McDowell, D. L. (2008). *J. Mech. Phys. Solids*, **56**, 1806–1830.

Turneure, S. J., Sharma, S. M., Volz, T. J., Winey, J. M. & Gupta, Y. M. (2017). *Sci. Adv.* **3**, eaao3561.

Wang, L., Cai, Y., He, A. M. & Luo, S. N. (2016). *Phys. Rev. B*, **93**, 174106.

Wang, L., Zhao, F., Zhao, F. P., Cai, Y., An, Q. & Luo, S. N. (2014). *J. Appl. Phys.* **115**, 053528.

Wehrenberg, C. E., McGonegle, D., Bolme, C., Higginbotham, A., Lazicki, A., Lee, H. J., Nagler, B., Park, H. S., Remington, B. A., Rudd, R. E., Sliwa, M., Suggit, M., Swift, D., Tavella, F., Zepeda-Ruiz, L. & Wark, J. S. (2017). *Nature*, **550**, 496–499.

Zhang, M., Li, L., Ding, J., Wu, Q., Wang, Y.-D., Almer, J., Guo, F. & Ren, Y. (2017). *Acta Mater.* **141**, 294–303.

Zhang, Y. Y., Tang, M. X., Cai, Y., E, J. C. & Luo, S. N. (2019). *J. Synchrotron Rad.* **26**, 413–421.

Zhu, Y., Kang, G. & Yu, C. (2017). *Int. J. Plast.* **95**, 191–215.